Entropic evidence for a Pomeranchuk effect in magic angle graphene

Asaf Rozen[1†], Jeong Min Park[2†], Uri Zondiner[1†], Yuan Cao[2†], Daniel Rodan-Legrain[2], Takashi Taniguchi[3], Kenji Watanabe[3], Yuval Oreg[1], Ady Stern[1], Erez Berg[1*], Pablo Jarillo-Herrero[2*] and Shahal Ilani[1*]

[1] *Department of Condensed Matter Physics, Weizmann Institute of Science, Rehovot 76100, Israel.*

[2] *Department of Physics, Massachusetts Institute of Technology, Cambridge, Massachusetts 02139, USA.*

[3] *National Institute for Materials Science, 1-1 Namiki, Tsukuba, 305-0044 Japan.*

[†] These authors contributed equally to the work.

[*]Correspondence to: erez.berg@weizmann.ac.il, pjarillo@mit.edu, shahal.ilani@weizmann.ac.il

In the 1950's, Pomeranchuk[1] predicted that, counterintuitively, liquid ^{3}He may solidify upon heating, due to a high excess spin entropy in the solid phase. Here, using both local and global electronic entropy and compressibility measurements, we show that an analogous effect occurs in magic angle twisted bilayer graphene[2–6]. Near a filling of one electron per moiré unit cell, we observe a dramatic increase in the electronic entropy to about $1k_B$ per unit cell. This large excess entropy is quenched by an in-plane magnetic field, pointing to its magnetic origin. A sharp drop in the compressibility as a function of the electron density, associated with a reset of the Fermi level back to the vicinity of the Dirac point, marks a clear boundary between two phases. We map this jump as a function of electron density, temperature, and magnetic field. This reveals a phase diagram that is consistent with a Pomeranchuk-like temperature- and field-driven transition from a low-entropy electronic liquid to a high-entropy correlated state with nearly-free magnetic moments. The correlated state features an unusual combination of seemingly contradictory properties, some associated with itinerant electrons, such as the absence of a thermodynamic gap, metallicity, and a Dirac-like compressibility, and others associated with localized moments, such as a large entropy and its disappearance with magnetic field. Moreover, the energy scales characterizing these two sets of properties are very different: whereas the compressibility jump onsets at $T \sim 30\mathrm{K}$, the bandwidth of magnetic excitations is $\sim 3\mathrm{K}$ or smaller. The hybrid nature of the new correlated state

and the large separation of energy scales have key implications for the physics of correlated states in twisted bilayer graphene.

Systems of strongly interacting fermions exhibit a competition between localization, minimizing the potential energy, and itineracy, minimizing kinetic energy. The advent of two-dimensional moiré systems, such as magic angle twisted bilayer graphene[2–6] (MATBG), allows studying this physics by controlling the ratio between the electronic interactions and bandwidth in a highly tunable way. When this ratio is large, electrons tend to localize and form Mott insulators[7,8]. When the bandwidth dominates, a Fermi liquid state is formed in which electrons are itinerant. MATBG is at the boundary between these two extremes, showing a host of fascinating electronic phases, including correlated insulators[3,9,10], Chern insulators[11–13], superconductors[4,9,10], and ferromagnets[14,15]. Scanning tunneling spectroscopy[16–19] and electronic compressibility measurements[20,21] indicate that in this system the strengths of the Coulomb interaction and the kinetic energy are indeed comparable. In this regime, there is an inherent tension between localized and itinerant descriptions of the physics. Moreover, the topological character[22–24] of the nearly-flat bands in MATBG implies that a simple "atomic" description, in which electrons are localized to individual moiré lattice sites, may not be appropriate. Instead, a picture analogous to that of quantum Hall ferromagnetism has been proposed[25–27]. Understanding this interplay between itineracy and localization, and the new physics that emerges from it, remains a major challenge.

In this work we find that, surprisingly, the correlated state in MATBG above a filling of one electron per moiré site has a hybrid nature, with some properties resembling those of an itinerant system, and others resembling those of localized electrons. At temperatures of a few Kelvin we measure unusually large excess entropy, which is rapidly suppressed by a moderate in-plane magnetic field. This suggests that even at such low temperatures, there are strongly fluctuating magnetic moments in the system, a behavior typically associated with local moments. On the other hand, our

measurements find that this state is metallic and has no thermodynamic gap, naturally fitting an itinerant picture.

The presence of fluctuating moments at temperatures much below the electronic bandwidth indicates the existence of a new, anomalously small energy scale associated with the bandwidth of magnetic excitations, which is an order of magnitude smaller than the scale where a jump appears in the compressibility[21,28]. This jump marks the boundary between the new state at filling factor $\nu > +1$ and the state at lower densities. By tracking the dependence of this boundary on temperature and magnetic field, we find that it exhibits an electronic analogue[29–32] of the famous Pomeranchuk effect[1] in ^{3}He. In that system, a transition from a Fermi liquid to a solid occurs upon increasing temperature, driven by the high nuclear spin entropy of the atoms in the solid. Similarly, we find that the new state above $\nu = +1$ is favored relative to the metallic state at $\nu < +1$ upon raising the temperature, due the former's high magnetic entropy. The transition near $\nu = +1$ can also be driven by an in-plane magnetic field that polarizes the free moments. (A related effect near $\nu = -1$ was proposed very recently, on the basis of transport measurements[33].) The hybrid state observed here, with itinerant electrons coexisting with strongly fluctuating magnetic moments, calls for a new understanding of electron correlations in MATBG.

Our data is measured using two independent techniques on two conceptually different devices. The bulk of the results are obtained from local measurements of the electronic entropy[34,35] and compressibility using a scanning nanotube single-electron transistor (SET) on hBN-encapsulated twisted bilayer device (Device 1, Fig. 1a). We focus on a large ($5\mu\text{m} \times 4\mu\text{m}$) region with an extremely homogenous twist angle that is close to the theoretical magic angle $\theta = 1.130 \pm 0.005$. Similar results are obtained from global entropy measurements using a monolayer graphene sensor (Device 2, Fig. 3a). Both methods have been described elsewhere[21,36].

Electronic compressibility and transport

The inverse compressibility, $d\mu/dn$, measured in Device 1 at $T = 15\mathrm{K}$ as a function of the filling factor, $\nu = n/(n_s/4)$ (where n_s corresponds to four electrons per moiré unit cell), is shown in Fig. 1b. As reported previously[21], sharp jumps in $d\mu/dn$ are observed close to integer ν's, reflecting Fermi surface reconstructions. These were termed Dirac revivals since they were interpreted as resets of partially filled energy bands back to near the Dirac point, leading to the decreased compressibility. The cascade of revivals is already very prominent at this relatively high temperature. Measurements of ρ_{xx} vs. ν at various temperatures (Fig. 1c) show insulating behavior at $\nu = 2,3$ and semi-metallic behavior at $\nu = 0$. As previously noted[37], ρ_{xx} shows a step-like increase across $\nu \approx 1$, which gradually disappears with decreasing temperature, markedly different than the behavior at other integer $\nu's$.

The unusual physics near $\nu = 1$ is revealed from the dependence of $d\mu/dn$ on temperature, T, and parallel magnetic field, $B_{\|}$. At low temperature and $B_{\|} = 0\mathrm{T}$ (Fig. 2a), the jump in $d\mu/dn$ occurs at ν slightly larger than 1. Increasing the temperature moves the jump towards a lower ν, and surprisingly, increases the magnitude of the jump rather than smearing it. Similar measurement with $B_{\|} = 12\mathrm{T}$ at low T (Fig. 2b) exhibits a much larger jump, which is also closer to $\nu = 1$. With increasing temperature, this jump remains close to $\nu = 1$, but oppositely to the $B_{\|} = 0\mathrm{T}$ case, reduces its amplitude and increases its width.

Local measurements of electronic entropy

The chemical potential, $\mu(\nu, T)$ (measured relative to that at charge neutrality), can be obtained by integrating $d\mu/dn$ over density (Fig. 2c,d). Visibly, μ depends strongly on T for a range of ν's. This is clearly seen when we plot μ vs. T at two representative ν's (Fig. 2c, inset). At $\nu = 0.2$, μ is practically independent of T (blue). In contrast, at $\nu = 0.9$ (red) μ is nearly constant until $T \sim 4\mathrm{K}$, and then decreases approximately linearly with T. At $\nu > 1.15$, μ is again nearly temperature independent. Comparing μ at $B_{\|} = 0\mathrm{T}$ (Fig. 2c) and $B_{\|} = 12\mathrm{T}$ (Fig. 2d) reveals a clear contrast:

whereas for $B_{\parallel} = 0\mathrm{T}$, μ is a decreasing function of temperature for $0.4 < \nu < 1.15$, for $B_{\parallel} = 12\mathrm{T}$, μ decreases with T for $\nu < 0.9$ and increases for $\nu > 0.9$.

These measurements allow us to directly determine the entropy of the system, by integrating Maxwell's relation: $\left(\frac{\partial s}{\partial \nu}\right)_T = -\left(\frac{\partial \mu}{\partial T}\right)_\nu$, to obtain $s(\nu, T)$ (where s is the entropy per moiré unit cell). For more details on this procedure see Supplementary Information section SI1. Fig. 2e shows $s(\nu)$ at $T \approx 10\mathrm{K}$ (obtained from the slope of μ vs. T in the range $T = 4.5\mathrm{K} - 15\mathrm{K}$), for $B_{\parallel} = 0\mathrm{T}, 4\mathrm{T}, 8\mathrm{T}$, and $12\mathrm{T}$. At $B_{\parallel} = 0\mathrm{T}$ the entropy is small at low $\nu's$, climbs close to $\nu = 1$, remains roughly constant between $\nu = 1$ and 2 at $s \approx 1.2k_B$, drops rapidly near $\nu = 2$, and decreases towards zero after $\nu = 3$. Clearly, the ν dependence of the entropy is qualitatively different from that of the compressibility: whereas the latter drops sharply near $\nu = 1$ (Fig. 2a), the former remains at a high value.

An important insight into the origin of this large entropy is given by its magnetic field dependence. As seen in Fig. 2e, the entropy above $\nu = 1$ depends strongly on $B_{\parallel}$. In particular, at $B_{\parallel} = 12\mathrm{T}$, most of the entropy between $\nu = 1$ and 2 is quenched. The inset shows $s(B_{\parallel} = 0\mathrm{T}) - s(B_{\parallel} = 12\mathrm{T})$ vs. ν (the purple shading indicates errorbars; see Supplementary Information SI1). The entropy difference increases sharply near $\nu = 1$, reaching a maximum of $0.85 \pm 0.1k_B$ between $\nu = 1$ and 2. To appreciate the significance of this value, recall that an entropy of $k_B \ln(2) \approx 0.7k_B$ corresponds to two degenerate states on each moiré unit cell. Moreover, in a Fermi liquid, we would expect a much weaker change of the entropy with $B_{\parallel}$ (Supplementary Information SI4), of the order of k_B times the ratio of the Zeeman energy (about $1\mathrm{meV}$ at $B_{\parallel} = 12\mathrm{T}$) to the bandwidth, estimated to be $W \sim 30\mathrm{meV}$ (see below). Finally, we observe that at $B_{\parallel} = 12\mathrm{T}$ the entropy shows a cascade of drops following each integer ν, similar to the revival drops observed in the compressibility (Supplementary Info. SI5), reproduced by the mean-field calculation (Supplementary Info. SI3). The dramatic quenching of entropy by moderate $B_{\parallel}$ strongly suggests a magnetic origin.

Global measurements of the entropy

To test the robustness of our results, we measured the entropy in a completely different setup, in which a sheet of monolayer graphene senses the chemical potential of MATBG, averaged over the entire device[36] (Fig. 3a). Fig. 3b shows the entropy extracted in three different temperature ranges. We see (inset) that the globally measured entropy for $T = 4\mathrm{K} - 16\mathrm{K}$ is in good agreement with the locally measured one over a similar range of temperatures, both in the overall shape, the magnitude of $s(\nu)$, and the detailed features. At elevated temperatures, the minimum in the entropy at $\nu = 0$ gradually fills in, evolving from a double-dome structure at low T (corresponding to the valence and conduction flat bands) to a single dome at high T. This dependence is qualitatively reproduced by a naïve calculation for a system of non-interacting electrons, whose density of states rises linearly from the charge neutrality point until the band edges (Fig. 3c). The merging of the domes in $s(\nu)$ occurs when the temperature exceeds a fraction of the bandwidth. Calibrating the bandwidth using the measured entropy at $T \approx 55\mathrm{K}$ gives $W \approx 30\mathrm{meV}$ (where W is the full bandwidth – from valence band bottom to conduction band top), in rough agreement with STM[16–19] and compressibility[36] experiments. This free-electron picture is of course invalid at low temperatures, where interactions are important. The measured $s(\nu)$ in the valence band is approximately a mirror image of $s(\nu)$ in the conduction band (Fig. 3b), although it is smaller and with less pronounced features. This is consistent with the weaker $d\mu/dn$ revivals observed in the valence band relative to the conduction band[21,36] (Supplementary Info. SI9).

Mapping the phase diagram

So far, we have shown a dramatic change in the magnetic entropy and compressibility near $\nu = 1$. This change may be due to a continuous buildup of electronic correlations. Alternatively, it can be interpreted as an underlying first-order phase transition between two distinct phases. Naively, one would then expect a

discontinuous jump in thermodynamic properties and hysteretic behavior across the transition, which are not observed. However, we note that a true first-order phase transition is forbidden in two dimensions in the presence of disorder or long-range Coulomb interactions[38], as these broaden the transition into a mesoscale coexistence region (Supplementary Info. S10). Experimentally, although the revival transition is very sharp and may be consistent with Coulomb- and/or disorder- smeared 1st order transition, we cannot rule out a sharp crossover or a higher order phase transition. Nevertheless, the sharpness of the rise of $d\mu/dn$ at the revival transition allows us to precisely track its filling factor, $\nu = \nu_R$(Fig. 4a), and map a phase diagram, which is naturally explained when this feature is interpreted as a proxy for a first-order transition.

The measured ν_R vs. $B_\parallel$ and T forms a surface in the $(\nu, B_\parallel, T)$ space (Fig. 4b) whose projections onto the $(\nu, B_\parallel)$ and (ν, T) are shown in Figs. 4c,d. At $T = 2.8\mathrm{K}$ and at low $B_\parallel$, ν_R depends weakly on $B_\parallel$, but decreases linearly above $B_\parallel \approx 4\mathrm{T}$ (Fig. 4c, blue). A similar crossover is observed at higher temperatures, but with a crossover $B_\parallel$ that increases with temperature. The T dependence of ν_R at $B_\parallel = 0\mathrm{T}$ (Fig. 4d) is linear at low temperatures and curves up at higher temperatures. As $B_\parallel$ increases, the curve shifts towards smaller ν's, and simultaneously its slope at low temperatures changes sign. At $B_\parallel = 12\mathrm{T}$, ν_R first increases with T, reaches a maximum at $T \approx 9\mathrm{K}$, and then decreases.

The phenomenology seen in Figs. 4b-d can be understood in terms of a first-order phase transition at $\nu = \nu_R$ between a Fermi liquid phase below ν_R, and a 'free moment' phase above it. The latter has a high concentration of free moments (about one per moiré site), coexisting with a low density of itinerant electrons. Within this framework, the shift of ν_R as a function of $B_\parallel$ and T reflects the magnetization and entropy differences between the two neighboring phases.

At $B_\parallel = 0\mathrm{T}$, the free moment phase has a higher entropy than the Fermi liquid, due to thermal fluctuations of the moments. Hence, the former becomes entropically-

favorable at high temperatures. This explains the observed decrease of ν_R with increasing T at low fields (Fig. 4d). Raising temperature at fixed ν may therefore drive a transition from the Fermi liquid to the free moments phase, an electronic analogue of the Pomeranchuk effect. As $B_{\parallel}$ increases and the Zeeman energy exceeds the temperature, the moments become nearly fully polarized and their entropy is quenched (as is observed directly in Fig. 2e). Consequently, at low temperatures and sufficiently high fields, the Fermi liquid phase is favored by raising the temperature. The trend reverses once the temperature exceeds the Zeeman energy. This explains the non-monotonic behavior of ν_R as a function of T, seen at $B_{\parallel} = 12\mathrm{T}$ in Fig. 4d. The main features of the phase boundary are qualitatively reproduced in a thermodynamic model of the two phases (Supplementary Info. SI7 and insets of Figs. 4b,c,d). Note that the experiment probes moments that couple to in-plane field. This includes Zeeman-coupled spins and may also include the valleys if their in-plane orbital moment is non-zero.

Discussion

The observation of free magnetic moments at surprisingly low temperatures has profound implications for the physics of MATBG. Low energy magnetic fluctuations are destructive for superconductivity and may be the limiting factor for the superconducting T_c. Moreover, increased scattering from fluctuating moments can account for the "strange metal" behavior reported over a broad range of temperatures[39,40].

An important question raised by our observations regards the origin of the free moments. Soft collective modes have been predicted in insulting states of MATBG[25–27], but our experiments show metallic behavior near $\nu = 1$. Moreover, the energy scale associated with the appearance of free moments is strikingly low ($3\mathrm{K}$ or less), much below the microscopic energy scales in the system. Understanding the state near $\nu = 1$, that combines behaviors associated with electron localization and itineracy, and its surprisingly low onset temperature, poses a key challenge for the theory of MATBG.

227

228

References

1. Pomeranchuk, I. On the thery of He3. *Zh.Eksp.Teor.Fiz* **20**, 919 (1950).
2. Bistritzer, R. & MacDonald, A. H. Moiré bands in twisted double-layer graphene. *Proc. Natl. Acad. Sci.* **108**, 12233–12237 (2011).
3. Cao, Y. *et al.* Correlated insulator behaviour at half-filling in magic-angle graphene superlattices. *Nature* **556**, 80–84 (2018).
4. Cao, Y. *et al.* Unconventional superconductivity in magic-angle graphene superlattices. *Nature* **556**, 43–50 (2018).
5. Li, G. *et al.* Observation of Van Hove singularities in twisted graphene layers. *Nat. Phys.* **6**, 109–113 (2010).
6. Suárez Morell, E., Correa, J. D., Vargas, P., Pacheco, M. & Barticevic, Z. Flat bands in slightly twisted bilayer graphene: Tight-binding calculations. *Phys. Rev. B* **82**, 121407 (2010).
7. Regan, E. C. *et al.* Mott and generalized Wigner crystal states in WSe2/WS2 moiré superlattices. *Nature* **579**, 359–363 (2020).
8. Tang, Y. *et al.* Simulation of Hubbard model physics in WSe2/WS2 moiré superlattices. *Nature* **579**, 353–358 (2020).
9. Yankowitz, M. *et al.* Tuning superconductivity in twisted bilayer graphene. *Science* **363**, 1059–1064 (2019).
10. Lu, X. *et al.* Superconductors, orbital magnets and correlated states in magic-angle bilayer graphene. *Nature* **574**, 653–657 (2019).
11. Nuckolls, K. P. *et al.* Strongly Correlated Chern Insulators in Magic-Angle Twisted Bilayer Graphene. *arXiv* 2007.03810 (2020).
12. Wu, S., Zhang, Z., Watanabe, K., Taniguchi, T. & Andrei, E. Y. Chern Insulators and Topological Flat-bands in Magic-angle Twisted Bilayer Graphene. *ArXiv* 2007.03725 (2020).
13. Das, I. *et al.* Symmetry broken Chern insulators and magic series of Rashba-like Landau level crossings in magic angle bilayer graphene. *Arxiv* 2007.13390 (2020).

14. Sharpe, A. L. *et al.* Emergent ferromagnetism near three-quarters filling in twisted bilayer graphene. *Science* **365**, 605–608 (2019).
15. Serlin, M. *et al.* Intrinsic quantized anomalous Hall effect in a moiré heterostructure. *Science* **367**, 900–903 (2020).
16. Kerelsky, A. *et al.* Maximized electron interactions at the magic angle in twisted bilayer graphene. *Nature* **572**, 95–100 (2019).
17. Xie, Y. *et al.* Spectroscopic signatures of many-body correlations in magic-angle twisted bilayer graphene. *Nature* **572**, 101–105 (2019).
18. Jiang, Y. *et al.* Charge order and broken rotational symmetry in magic-angle twisted bilayer graphene. *Nature* **573**, 91–95 (2019).
19. Choi, Y. *et al.* Electronic correlations in twisted bilayer graphene near the magic angle. *Nat. Phys.* **15**, 1174–1180 (2019).
20. Tomarken, S. L. *et al.* Electronic Compressibility of Magic-Angle Graphene Superlattices. *Phys. Rev. Lett.* **123**, 046601 (2019).
21. Zondiner, U. *et al.* Cascade of phase transitions and Dirac revivals in magic-angle graphene. *Nature* **582**, 203–208 (2020).
22. Po, H. C., Zou, L., Vishwanath, A. & Senthil, T. Origin of Mott insulating behavior and superconductivity in twisted bilayer graphene. *Phys. Rev. X* **8**, 031089 (2018).
23. Song, Z. *et al.* All Magic Angles in Twisted Bilayer Graphene are Topological. *Phys. Rev. Lett.* **123**, 036401 (2019).
24. Ahn, J., Park, S. & Yang, B.-J. Failure of Nielsen-Ninomiya Theorem and Fragile Topology in Two-Dimensional Systems with Space-Time Inversion Symmetry: Application to Twisted Bilayer Graphene at Magic Angle. *Phys. Rev. X* **9**, 021013 (2019).
25. Bultinck, N. *et al.* Ground State and Hidden Symmetry of Magic-Angle Graphene at Even Integer Filling. *Phys. Rev. X* **10**, 031034 (2020).
26. Ajesh Kumar, Ming Xie, A. H. MacDonald,Lattice Collective Modes from a Continuum Model of Magic-Angle Twisted Bilayer Graphene. ArXiv:2010.05946

27. Wu, F. & Das Sarma, S. Collective Excitations of Quantum Anomalous Hall Ferromagnets in Twisted Bilayer Graphene. *Phys. Rev. Lett.* **124**, 046403 (2020).
28. Wong, D. *et al.* Cascade of electronic transitions in magic-angle twisted bilayer graphene. *Nature* **582**, 198–202 (2020).
29. McWhan, D. B. *et al.* Electronic Specific Heat of Metallic Ti-Doped V2O3. *Phys. Rev. Lett.* **27**, 941–943 (1971).
30. Spivak, B. & Kivelson, S. A. Phases intermediate between a two-dimensional electron liquid and Wigner crystal. *Phys. Rev. B* **70**, 155114 (2004).
31. Continentino, M. A., Ferreira, A. S., Pagliuso, P. G., Rettori, C. & Sarrao, J. L. Solid state Pomeranchuk effect. *Phys. B Condens. Matter* **359**–**361**, 744–746 (2005).
32. Pustogow, A. *et al.* Quantum spin liquids unveil the genuine Mott state. *Nat. Mater.* **17**, 773–777 (2018).
33. Saito, Y. *et al.* Isospin Pomeranchuk effect and the entropy of collective excitations in twisted bilayer graphene. *ArXiv* 2008.10830 (2020).
34. Kuntsevich, A. Y., Tupikov, Y. V, Pudalov, V. M. & Burmistrov, I. S. Strongly correlated two-dimensional plasma explored from entropy measurements. *Nat. Commun.* **6**, 7298 (2015).
35. Hartman, N. *et al.* Direct entropy measurement in a mesoscopic quantum system. *Nat. Phys.* **14**, 1083–1086 (2018).
36. Park, J. M., Cao, Y., Watanabe, K., Taniguchi, T. & Jarillo-Herrero, P. Flavour Hund's Coupling, Correlated Chern Gaps, and Diffusivity in Moir'e Flat Bands. *Arxiv* 2008.12296 (2020).
37. Chen, S. *et al.* Electrically tunable correlated and topological states in twisted monolayer-bilayer graphene. *Arxiv* 2004.11340 (2020).
38. Spivak, B. & Kivelson, S. A. Transport in two dimensional electronic micro-emulsions. *Ann. Phys.* **321**, 2071–2115 (2006).
39. Cao, Y. *et al.* Strange Metal in Magic-Angle Graphene with near Planckian Dissipation. *Phys. Rev. Lett.* **124**, 076801 (2020).

40. Polshyn, H. *et al.* Large linear-in-temperature resistivity in twisted bilayer graphene. *Nat. Phys.* **15**, 1011–1016 (2019).
41. Uri, A. *et al.* Mapping the twist-angle disorder and Landau levels in magic-angle graphene. *Nature* **581**, 47–52 (2020).

Acknowledgements: We thank Ehud Altman, Eva Andrei, Eslam Khalaf, Steve Kivelson, Sankar Das Sarma, Gal Shavit, Joey Sulpizio, Senthil Todadri, Aviram Uri, Ashvin Vishwanath, Michael Zaletel and Eli Zeldov for useful suggestions. E.B. is grateful to Andrea Young for drawing his attention to the unusual physics near $\nu = \pm 1$, sharing his unpublished data, and for a collaboration on a related experimental and theoretical work[33], proposing that a similar effect to the one discussed here occurs near $\nu = -1$, based on transport measurements. In this work, in contrast, we measured the entropy directly, and mapped the entire phase diagram near $\nu = 1$ using compressibility measurements. Work at Weizmann was supported by the Leona M. and Harry B. Helmsley Charitable Trust grant, ISF grants (712539 & 13335/16), Deloro award, Sagol Weizmann-MIT Bridge program, the ERC-Cog (See-1D-Qmatter, no. 647413), the ISF Research Grants in Quantum Technologies and Science Program (994/19 & 2074/19), the DFG (CRC/Transregio 183), ERC-Cog (HQMAT, no. 817799), EU Horizon 2020 (LEGOTOP 788715) and the Binational Science Foundation (NSF/BMR-BSF grant 2018643). Work at MIT was primarily supported by the US Department of Energy (DOE), Office of Basic Energy Sciences (BES), Division of Materials Sciences and Engineering under Award DE-SC0001819 (J.M.P.). Help with transport measurements and data analysis were supported by the National Science Foundation (DMR-1809802), and the STC Center for Integrated Quantum Materials (NSF Grant No. DMR-1231319) (Y.C.). P.J-H acknowledges support from the Gordon and Betty Moore Foundation's EPiQS Initiative through Grant GBMF9643 and partial support by the Fundación Ramón Areces. The development of new nanofabrication and characterization techniques enabling this work has been supported by the US DOE Office of Science, BES, under award DE-

SC0019300. K.W. and T.T. acknowledge support from the Elemental Strategy Initiative conducted by the MEXT, Japan, Grant Number JPMXP0112101001, JSPS KAKENHI Grant Numbers JP20H00354 and the CREST(JPMJCR15F3), JST. This work made use of the Materials Research Science and Engineering Center Shared Experimental Facilities supported by the National Science Foundation (DMR-0819762) and of Harvard's Center for Nanoscale Systems, supported by the NSF (ECS-0335765).

Author Contributions: A.R., J.M.P, U.Z., Y.C., P.J-H. and S.I. designed the experiment. A.R.,U.Z., performed the scanning SET experiments, J.M.P, Y.C. performed the monolayer graphene sensing experiments. D.R-L. and Y.C. fabricated the twisted bilayer graphene devices. A.R., J.M.P, U.Z., Y.C., P.J-H. and S. I. analyzed the data. E.B., Y.O. and A.S. wrote the theoretical model. K.W. and T.T. supplied the hBN crystals. A.R., J.M.P, U.Z., Y.C., Y.O., A.S., E.B., P.J-H. and S.I. wrote the manuscript.

Competing interests: The authors declare no competing interests.

Figure 1: Experimental setup and device characterization. a. A nanotube-based single electron transistor (SET) is used to measure the local electronic compressibility and entropy of magic angle twisted bilayer graphene (MATBG). The MATBG is encapsulated between top and bottom h-BN layers (not shown) and has a metallic back-gate. By monitoring the current through the SET, we track changes in the MATBG chemical potential, $d\mu$, in response to a density modulation, dn, produced by an a.c. voltage on the back-gate[21], δV_{BG}. A d.c. back-gate voltage, V_{BG}, sets the overall carrier density in the MATBG, *n*. Some of the measurements are performed in a parallel magnetic field, $B_{\|}$ (indicated). **b.** Inverse compressibility, $d\mu/dn$, measured as a function of the moiré lattice filling factor, $\nu = n/(n_s/4)$, at $T = 15K$ (n_s is the density that correspond to 4 electrons per moiré site). Measurements are done on a large spatial domain ($\sim 5\mu m \times 4\mu m$) throughout which the twist angle is extremely homogenous, $\theta = 1.130^{\circ} \pm 0.005$ (measured by spatial mapping of the V_{BG} that corresponds to n_s, as in Refs. [21,41]). As seen previously[21], a jump of $d\mu/dn$ appears near all integer filling factors. This jump corresponds to a Fermi surface reconstruction, in which some combination of the spin/valley flavors filling is reset back to near the charge neutrality point, and correspondingly $d\mu/dn$ shows a cascade of sawtooth features as a function of density. The trace is measured at $T = 15\mathrm{K}$, showing that even at this high temperature this sawtooth cascade is well developed **c.** Two-probe resistance, R, measured as a function of ν and temperature. Notice that unlike the inverse compressibility, which measures a local quantity, the resistance gives an averaged result over domains with different twist angle. Therefore, the resistance maxima are slightly shifted from the usual integer ν values, probably because another domain with a small difference in twist angle dominates the transport characteristics globally.

Figure 2: Measurement of large magnetic entropy above $\boldsymbol{\nu = 1}$. a. Inverse compressibility, $d\mu/dn$, as a function of ν, near $\nu = 1$, measured at zero parallel magnetic field, $B_{\|} = 0T$, and at several temperatures. With increasing T, the jump in

$d\mu/dn$ moves toward lower ν and becomes stronger. **b.** Same measurement done at $B_{\parallel} \approx 12T$. Here, opposite to the zero-field case, increasing T reduces the magnitude of the $d\mu/dn$ jump, as expected from thermal smearing. **c.** The chemical potential $\mu(\nu)$ (relative to that of the charge neutrality point) at $B_{\parallel} = 0T$, obtained by integrating the $d\mu/dn$ signal in panel a with respect to n. Inset: $\mu(T,\nu) - \mu(T = 2.8K,\nu)$ for $\nu = 0.2$ (blue) and $\nu = 0.9$ (red). At $\nu = 0.2$ the chemical potential is nearly temperature independent, whereas at $\nu = 0.9$ it is roughly constant until $T \sim 4\mathrm{K}$ and then start decreasing approximately linearly with T. **d.** Similar to c, but at $B_{\parallel} = 12T$. In contrast to the zero-field case, here, below $\nu \approx 0.9$, μ decreases with T while above $\nu \approx 0.9$ μ increases with T. **e.** The electronic entropy in units of k_B per moiré unit cell, as a function of ν at $T \approx 10\mathrm{K}$ and at various parallel magnetic fields, $B_{\parallel} = 0,4,8,12\mathrm{T}$. To obtain the entropy we determine the partial derivative $(\partial\mu/\partial T)_{\nu,B_{\parallel}}$ from a linear fit to the measured μ vs. T in the range $T = 4.5\mathrm{K} - 15\mathrm{K}$. The entropy per moiré cell is then obtained by integrating Maxwell's relation: $(\partial s/\partial \nu)_{T,B_{\parallel}} = -(\partial\mu/\partial T)_{\nu,B_{\parallel}}$, over ν (see Supp Info. for details) . At $B_{\parallel} = 0$ the entropy climbs rapidly near $\nu = 1$ to a value of $1.2k_B$ per moiré cell. Inset: the difference between the entropies at low and high fields, $s(B_{\parallel} = 0\mathrm{T}) - s(B_{\parallel} = 12\mathrm{T})$. The purple shading shows the estimated error bar.

Figure 3: Temperature dependence of the Entropy. a. Experimental setup for measuring the global entropy, averaged over the entire device[36]. The device consists of MATBG and a monolayer graphene (MLG) sensor layer, separated by an ultrathin ($1\ nm$) layer of h-BN (not shown), as well as top and bottom metallic gates. By balancing the electrochemical potential of the adjacent layers in the device, we can obtain the relationship between the density and chemical potential of MATBG and MLG and the gate voltages applied to the system. In the special case where the density of MLG is zero, i.e. at its charge neutrality point, the chemical potential of MATBG is directly proportional to the voltage applied to the top gate. This technique allows us to reliably extract the chemical potential and entropy of MATBG at temperatures up to 70 K. **b.**

The measured entropy, in units of k_B per moiré unit cell, as a function of ν at three different temperature ranges (top legend). The entropy derivative, $ds/d\nu$, is obtained from a linear fit to μ vs. T in the corresponding temperature range, and is then integrated over ν to yield the entropy per moiré unit cell (similar to Fig. 2e). Inset: comparison between the ν dependences of the entropies, measured at the low temperature range, obtained from local and global measurements. **c.** The entropy as a function of ν and T calculated for a system of four degenerate non-interacting Dirac bands (whose density of states climbs linearly with energy from the Dirac point to the end of the conduction or the valence band). The color-coded lines show the curves whose temperatures correspond to the mean of the temperature ranges of the experimental curves. The gray lines represent the entire evolution from zero temperature to high temperature, where the entropy saturates on a value of $8ln(2) \approx 5.5$, where the factor 8 reflects the total number of energy bands. A bandwidth of $W = 30meV$ is chosen such that the calculated value of the entropy at the highest temperature roughly matches the one obtained from the measured curve at the same temperature.

Figure 4: Experimental phase diagram. a. The inverse compressibility, $d\mu/dn$, measured as a function of ν near $\nu = 1$, at several values of parallel magnetic field, $B_{\parallel}$. We track the filling factor that corresponds to the center the jump in $d\mu/dn$ (labeled ν_R). Visibly, the application of $B_{\parallel}$ pushes ν_R to lower values. **b.** Measured ν_R as a function of $B_{\parallel}$ and T, plotted as dots in the $(\nu, B_{\parallel}, T)$ space (the dots are colored by their temperature). The dashed lines are polynomial fits to the dots at constant $B_{\parallel}$ or constant T. Inset: the same surface calculated from a simple model that assumes a transition between a Fermi liquid and a metallic phase that contains one free moments per moiré site (see text). **c.** Projection of the data in panel b onto the $(\nu, B_{\parallel})$ plane, showing the dependence of ν_R on $B_{\parallel}$ for various temperatures. At low fields, ν_R is independent of field but it becomes linear in $B_{\parallel}$ at high fields, a behavior expected from

the field polarization of free moments (see text). Inset: curves calculated from the model. **d.** Projection onto the (ν, T) plane, showing the dependence of ν_R on T for various magnetic fields. At $B_{\parallel} = 0T$, ν_R is linear in T at small T 's and then curves up at higher T's. At high magnetic field, the dependence of ν_R on T becomes non-monotonic. Inset: curves calculated from the model.

Data availability: The data in the main text is available in https://github.com/erezberg/pomeranchuk_data
The code used in this work is available in https://github.com/erezberg/pomeranchuk_tblg_theory

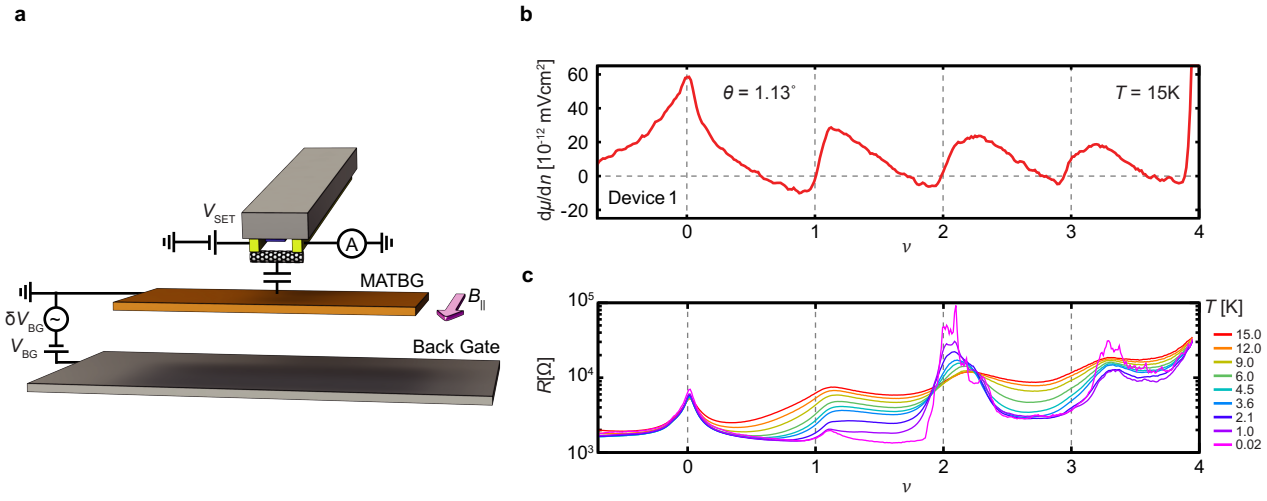
a
b
c
V_{SET}
A
MATBG
$B_{\parallel}$
δV_{BG}
V_{BG}
Back Gate
$d\mu/dn$ [10^{-12} mVcm^2]
θ = 1.13°
T = 15K
Device 1
ν
$R[\Omega]$
T [K]
15.0
12.0
9.0
6.0
4.5
3.6
2.1
1.0
0.02

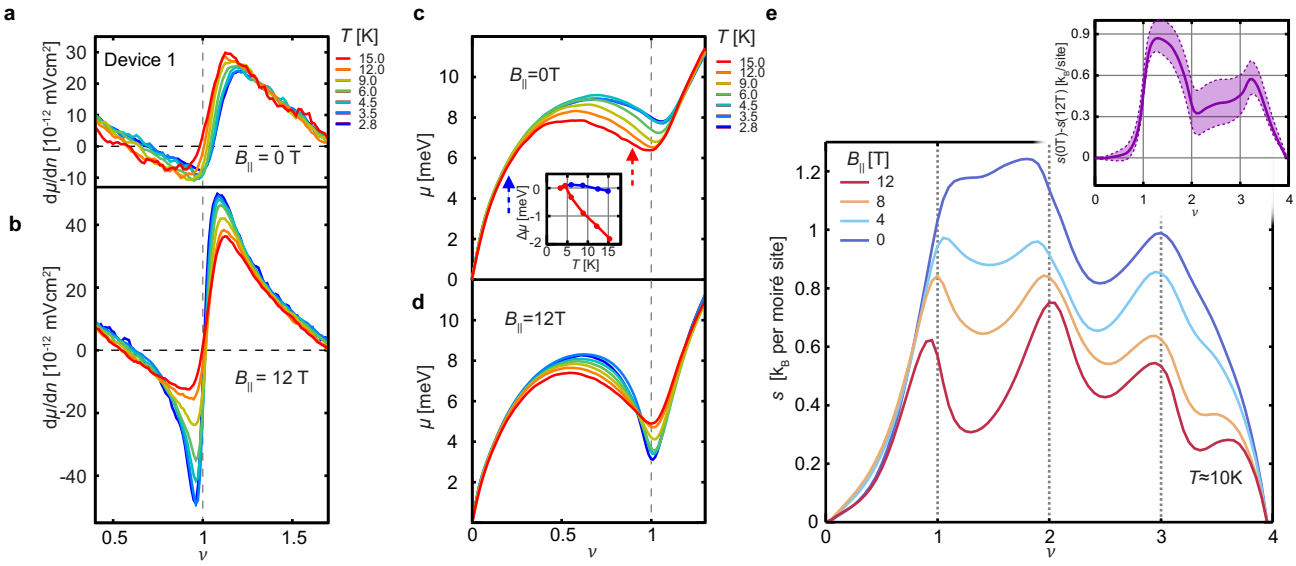
a
b
c
d
e
Device 1
$B_{||}$ = 0 T
$B_{||}$ = 12 T
$B_{||}$=0T
$B_{||}$=12T
T [K]
15.0
12.0
9.0
6.0
4.5
3.5
2.8
dμ/dn [10⁻¹² mVcm²]
μ [meV]
Δμ [meV]
T [K]
ν
$B_{||}$ [T]
12
8
4
0
s [k_B per moiré site]
s(0T)-s(12T) [k_B/site]
T≈10K

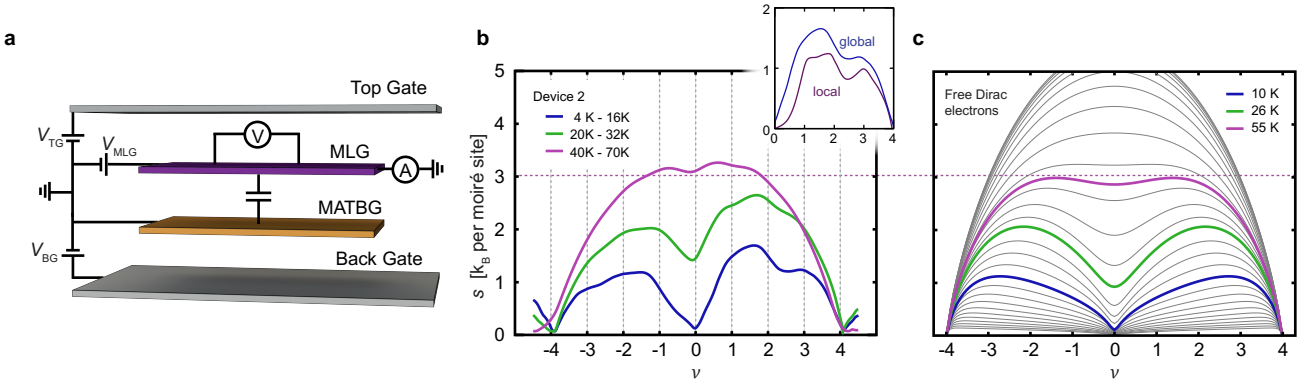
a
Top Gate
V_{TG}
V_{MLG}
V
MLG
A
MATBG
V_{BG}
Back Gate
b
Device 2
4 K - 16K
20K - 32K
40K - 70K
s [k_B per moiré site]
ν
global
local
c
Free Dirac electrons
10 K
26 K
55 K
ν

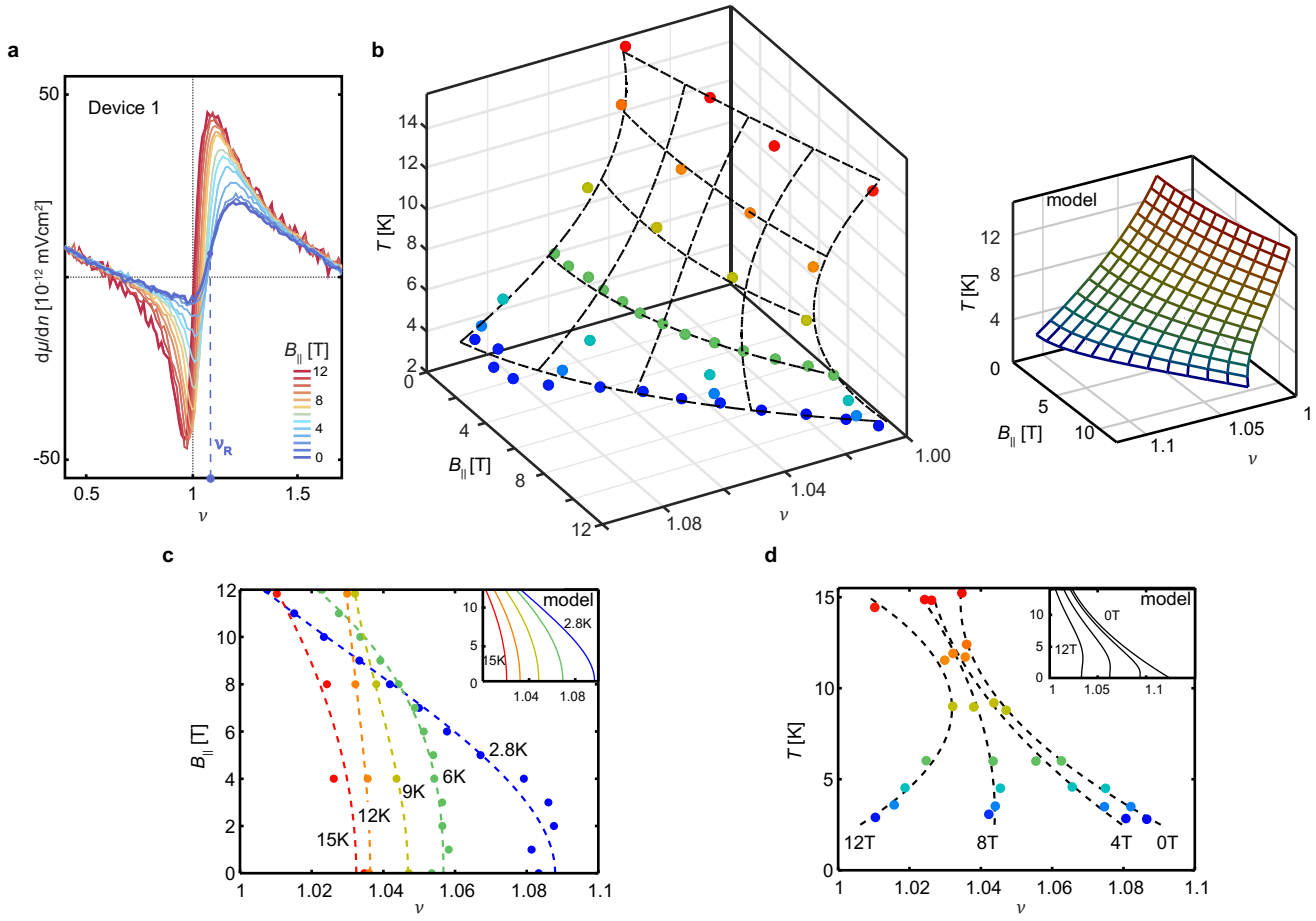
a
Device 1
50
-50
dμ/dn [10⁻¹² mVcm²]
0.5
1
1.5
ν
B∥ [T]
12
8
4
0
νR
b
T [K]
14
12
10
8
6
4
2
0
B∥ [T]
4
8
12
1.00
1.04
1.08
ν
model
T [K]
12
8
4
0
B∥ [T]
5
10
1.1
1.05
1
ν
c
B∥ [T]
12
10
8
6
4
2
0
1
1.02
1.04
1.06
1.08
1.1
ν
2.8K
6K
9K
12K
15K
model
10
5
0
1.04
1.08
d
T [K]
15
10
5
0
1
1.02
1.04
1.06
1.08
1.1
ν
12T
8T
4T
0T
model
10
5
0
12T
0T
1
1.05
1.1

Supplementary materials for:

Entropic evidence for a Pomeranchuk effect in Magic Angle graphene

Asaf Rozen[†], Jeong Min Park[†], Uri Zondiner[†], Yuan Cao[†], Daniel Rodan-Legrain, Takashi Taniguchi, Kenji Watanabe, Yuval Oreg, Ady Stern, Erez Berg[*], P. Jarillo-Herrero [*] and Shahal Ilani[*]

Contents

SI1. Extraction of the entropy

In both the local and global measurements, we determine the entropy using a Maxwell relation, relating the partial derivatives of the entropy with respect to the filling factor to that of the chemical potential with respect to temperature:

$$(\partial s/\partial \nu)_{T,B_\parallel} = -(\partial \mu/\partial T)_{B_\parallel,\nu}$$

where s is the entropy per moiré unit cell. In the global measurements, we probe the chemical potential of the MATBG directly using a monolayer graphene sensor. The measurement determines the chemical potential relative to that at the charge neutrality point (CNP):

$$\Delta\mu(\nu,T,B_\parallel) = \mu(\nu,T,B_\parallel) - \mu_{CNP}(T,B_\parallel).$$

In the local measurements, we use a nanotube single electron transistor to measure the inverse compressibility and integrate it over the density, to obtain the same quantity:

$$\Delta\mu(\nu,T,B_\parallel) = \mu(\nu,T,B_\parallel) - \mu_{CNP}(T,B_\parallel) = \int_0^n (\partial\mu/\partial n)_{B_\parallel,T}\, dn'.$$

In these measurements, the inverse compressibility is probed at typical frequencies of few hundred Hz, and with an excitation $\delta V_{BG} = 40mV$ on the back gate, chosen to be small enough as to not smear essential features.

The entropy then follows from:

$$\mathrm{s}(\nu,T,B_\parallel) = \int_0^\nu (\partial s/\partial \nu)_{T,B_\parallel}\, d\nu' = -\int_0^\nu (\partial\mu/\partial T)_{B_\parallel,\nu}\, d\nu'$$
$$= -\int_0^\nu \frac{d(\Delta\mu)}{dT} d\nu' - \int_0^\nu \frac{d\mu_{CNP}}{dT} d\nu'$$

The first term provides the ν-dependent part of the entropy. The second one, which we do not measure directly, adds a linear term in ν. The value of this constant is determined by making the assumption that inside the gap separating the conduction flat band and the higher dispersive band, namely at $\nu = 4$, the electronic entropy is zero. To see why this assumption is justified we note that inside a gap, the electronic entropy is given by $s = 16k_B \frac{E_g}{W} e^{-\frac{E_g}{2k_B T}}$ (where W is the width of the flat band, and E_g is the size of the gap to the dispersive band). Our compressibility measures directly the size of the gap to be $E_g \approx 30meV$, and estimate the bandwidth to be of similar magnitude $W \approx 30 - 40meV$. The entropy in such gap at $T \approx 10\mathrm{K}$

is $s \approx 4 \cdot 10^{-7} k_B$, making our assumption well justified for the relevant temperatures reported in the paper.

We note that the bandwidth of the flat bands obtained from this fit is significantly larger than the theoretical predications, and that this is consistent with the large bandwidths observed in all existing experiments: STM experiments (Ref 16-19 in the main text) give bandwidths in the range of $22meV - 55meV$ and compressibility measurements (Ref 21, 26 in main text) give $40meV - 55meV$. The somewhat larger estimate of bandwidth from compressibility, might reflect the fact that when the mixing to the high-energy dispersive bands is not negligible, the bandwidth extracted from compressibility may increase slightly by the effects of interactions.

Fig. S1a shows the derivative of the entropy per electron with respect to ν for three different temperature ranges, from the measurements done in Device 2. using the global measurements. We removed a constant background in *ds/dν* (ν) to account for the variation of μ with *T* at charge neutrality, such that the entropy at $\nu = \pm 4$ is zero. For each temperature range, μ was assumed to be linearly dependent on T at a given ν. The confidence bound of 95% is shown for this linear fitting process. The entropy obtained after integration is shown in Fig. S1b. The error highlighted bands show the propagated uncertainty in this integration process.

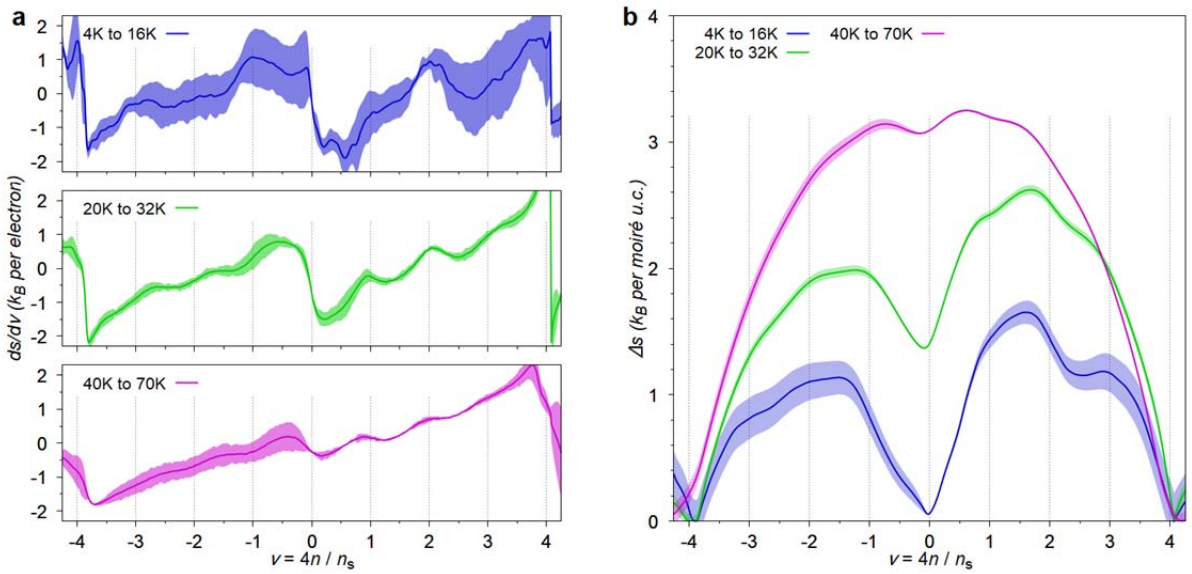

Fig. S1: Extraction of entropy in Device 2 for different temperatures. (a) Derivative of entropy with respect to ν obtained from Maxwell's relation $(\partial s/\partial \nu)_{T,B_\parallel} = -(\partial \mu/\partial T)_{B_\parallel,\nu}$ for three temperature ranges spanning 4 K to 70 K. (b) Entropy change Δs per moiré unit cell with respect to the band insulators at $\nu = \pm 4$.

In the scanning SET measurements, we get an additional small component of parasitic capacitance between the SET and the back-gate. This results from the fact that our SET scans at a finite height (hundreds on *nm*'s) above the MATBG. This parasitic capacitance adds a background to the measured inverse compressibility of the order of $d\mu/dV < 10^{-4}$. In the estimation of the entropy this gets doubly integrated yielding a term that depends quadratically on ν. We remove this term by assuming that the entropy at $\nu = 0$ is also zero (in addition to assuming it is zero at $\nu = 4$ as discussed above). As seen in the global entropy measurements (Fig. 3b and S1b), the entropy curve that correspond to the temperature range $T = 4\mathrm{K} - 16\mathrm{K}$ (blue) shows that the entropy at $\nu = 0$ is smaller than $0.1k_B$. Since local entropy measurements are performed only in this temperature range, the assumption that $s = 0$ at $\nu = 0$ is justified.

To determine the uncertainty in the local measurements of the entropy (Fig. 2e in the main text), we first extract the noise level in our measured $d\mu/dn$. We then add to our measured compressibility signal randomly distributed noise with the experimental noise variance and see how it changes the resulting entropy curve. Repeating this over a statistically significant instances of random noise gives us the error bars in our determined entropy, which are shown in Fig. S2, for the traces taken at different parallel magnetic fields (as in Fig. 2e in the main text).

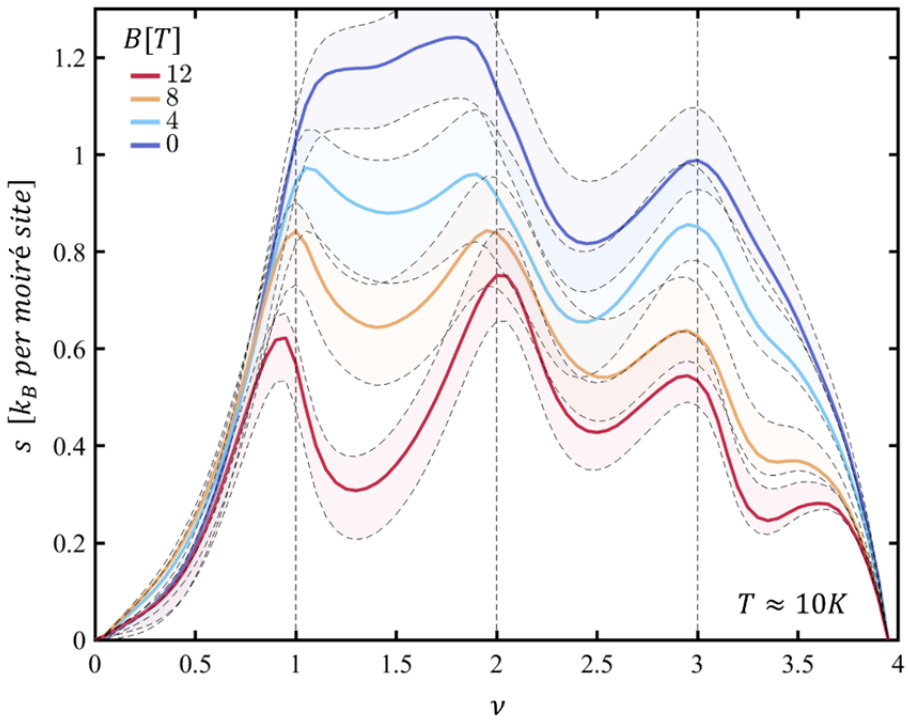

Fig. S2: Errorbars of the measured local entropy. Solid lines show s vs. ν for serval values of $B_{\parallel}$. The shaded bands around each curves give the 1 sigma errorbars (see the text in this Supplementary section for details).

SI2. Entropy of non-Interacting Dirac electrons

To get a rough understanding of the overall ν dependence of the measured entropy at high temperatures, it is useful to compare it to the entropy in a system of non-interacting Dirac bands. The curves in Fig. 3c in the main text were obtained for such a model with the a single-particle density of states that rises linearly from zero at the charge neutrality point up to the band top and bottom at $\pm W/2$, where W is the bandwidth. The density of states $\rho(\varepsilon)$ for each spin/valley flavor is given by:

$$\rho(\varepsilon) = \frac{8|\varepsilon|}{W^2}\Theta\left(\frac{W}{2} - |\varepsilon|\right), \quad (1)$$

where $\Theta(x)$ is the Heaviside step function. The entropy per unit cell is then given by:

$$s(\nu,T) = -g_f k_B \int_{-\infty}^{\infty} d\varepsilon \rho(\varepsilon)\{n_F(\varepsilon)\ln[n_F(\varepsilon)] + [1-n_F(\varepsilon)]\ln[1-n_F(\varepsilon)]\}. \quad (2)$$

Here, $g_f = 4$ is the number of spin/valley flavors, $n_F(\varepsilon) = 1/(1+e^{(\varepsilon-\mu)/T})$ is the Fermi-Dirac distribution, and the chemical potential is determined by solving the equation for the filling factor ν, given by:

$$\nu = g_f\left[\int_{-\infty}^{\infty} d\varepsilon \rho(\varepsilon) n_F(\varepsilon) - 1\right]. \quad (3)$$

Solving Eq. (3) for $\mu(\nu,T)$ and inserting the result into (2) gives $s(\nu,T)$ shown in Fig. 3c of the main text.

SI3. Entropy in mean-field Dirac revival model

In Refs.[1,2], we have used a simple mean-field model to describe the Dirac revival features in the compressibility. At zero temperature, this model features a cascade of phase transitions upon increasing the electron density, where the spin and valley symmetries are successively broken. At each transition, electrons of one flavor become more populated than the others. The minority flavors' densities reset to the vicinity of the charge neutrality point. This causes a sharp drop in the density of states at the Fermi level, reviving the Dirac-like density dependence of the inverse compressibility near each integer filling factor. Hence, we termed this phenomenon "Dirac revival transitions".

Here, we present a calculation of the entropy as a function of density and in-plane magnetic field within the same mean-field model. The model consists of four flavors of electrons (two valleys and two spins), each with a single-particle density of states $\rho(\varepsilon)$. The interaction, of strength U, is assumed to be local in real space and featureless in flavor space. The Hamiltonian is written as

$$H = \sum_{\mathbf{k},\alpha,n} (\varepsilon_{\alpha n\mathbf{k}} - \mu)\psi^{\dagger}_{\alpha n\mathbf{k}}\psi_{\alpha n\mathbf{k}} + H_{\text{int}}, \quad (4)$$

where $\alpha = \{K\uparrow, K\downarrow, K'\uparrow, K'\downarrow\}$ is a spin/flavor index, $n = 1,2$ labels the conduction and valence bands, $\varepsilon_{\alpha n\mathbf{k}}$ are the band dispersions (that are valley and n dependent but spin independent), and the interaction Hamiltonian is given by:

$$H_{\text{int}} = \frac{U}{2N}\sum_{\alpha\neq\beta}\sum_{\{n_i\},\{\mathbf{k}_i\},\mathbf{G}}\delta_{\mathbf{k}_1+\mathbf{k}_2-\mathbf{k}_3-\mathbf{k}_4+\mathbf{G}}\,\psi^{\dagger}_{\alpha n_1\mathbf{k}_1}\psi^{\dagger}_{\beta n_2\mathbf{k}_2}\psi_{\beta n_3\mathbf{k}_3}\psi_{\alpha n_4\mathbf{k}_4}. \quad (5)$$

Here, N is the number of unit cells, and $\mathbf{G}$ is a reciprocal lattice vector. The interaction couples only electrons of different spin/valley flavors, since it is assumed to be delta function-like in real space. Then, by the Pauli principle, two electrons of the same spin and valley cannot occupy the same point in real space, and do not interact. This captures the exchange part of the interaction, which favors spin or valley polarization. Including an intra-flavor term J, as in Ref[2]., does not change the results for the entropy shown below.

We analyze the system within a Hartree-Fock mean-field approximation, allowing for an arbitrary filling of each flavor, but no other form of broken symmetry. We use a mean-field Hamiltonian of the form:

$$H_{\text{MF}} = \sum_{\mathbf{k},\alpha,n}(\varepsilon_{\alpha n\mathbf{k}} - \mu - \mu_\alpha)\psi^{\dagger}_{\alpha n\mathbf{k}}\psi_{\alpha n\mathbf{k}}, \quad (6)$$

with variational parameters μ_α, and minimize the grand potential of the trial density matrix $\hat{\rho} = \frac{e^{-H_{MF}/T}}{\text{Tr}[e^{-H_{MF}/T}]}$. The variational grand potential per unit cell is given by

$$\Omega_{\text{MF}} = \sum_\alpha f(\mu_\alpha+\mu) + \frac{U}{2}\sum_{\alpha\neq\beta}\nu(\mu_\alpha+\mu)\nu(\mu_\beta+\mu) + \sum_\alpha \mu_\alpha\nu(\mu_\alpha+\mu) \quad (7)$$

where

$$f(\mu) = -T\int_{-\infty}^{\infty} d\varepsilon\,\rho(\varepsilon)\left[\log\left(1+e^{-\frac{\varepsilon-\mu}{T}}\right) + \frac{\varepsilon-\mu}{T}\Theta(-\varepsilon)\right],$$

$$\nu(\mu) = \int_{-\infty}^{\infty} d\varepsilon\,\rho(\varepsilon)\left(\frac{1}{1+e^{(\varepsilon-\mu)/T}} - \Theta(-\varepsilon)\right).$$

Here, $\rho(\varepsilon) = \frac{1}{N}\sum_{\mathbf{k}}\delta(\varepsilon-\varepsilon_{\mathbf{k}})$ is the density of states of each flavor. Minimizing Eq. (6) with respect to μ_α, we obtain a variational estimate for $\Omega(\mu, T)$. The entropy can then be obtained

though $s = -\frac{\partial \Omega}{\partial T}$. Following Ref[1], we use a simple linear model for the density of states, given in Eq. (1). Using different models for the density of states does not alter the results qualitatively.

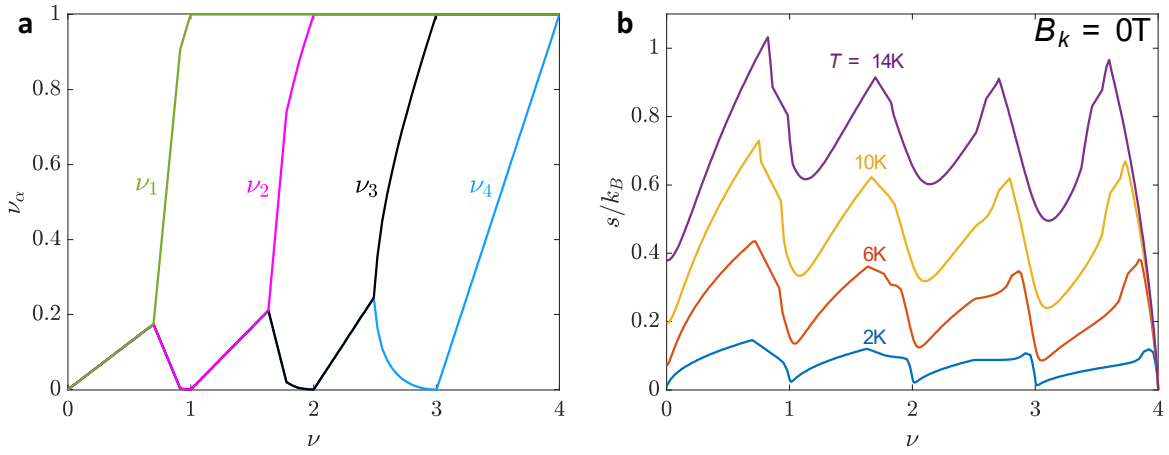

Figure S3: Mean-field calculation. a. Partial occupations ν_α of each valley/spin flavor as a function of total filling factor ν, at $T = 0$, $B_\parallel = 0$, showing a cascade of flavor symmetry breaking transitions near each integer filling. **b.** Entropy as a function of ν at $B_\parallel = 0$, for different temperatures. The dips in the entropy correspond to the resetting of some of the spin/valley flavors back to the charge neutrality point ($\nu_\alpha = 0$), while others are fully filled. At these points the density of states at the Fermi level is minimal.

We expect that at low temperatures, this approximation, built on a density matrix corresponding to a non-interacting Hamiltonian with self-consistently determined μ_α's, will exhibit an entropy that is essentially $s = \frac{\pi^2}{3}\sum_\alpha \rho(\mu + \mu_\alpha)T$. Hence, the entropy is proportional to the total density of states at the Fermi level.

Fig. S3a shows the partial filling factors of each flavor as a function of the total filling factor at zero temperature, choosing $W = 2U = 300\text{K}$. The results do not change qualitatively for different values of U/W, as long as $2U$ and W are comparable[1,2]. As seen in the figure, near charge neutrality, all four flavors start filling equally as the density is raised. Before $\nu = 1$ is reached, a phase transition occurs, in which one flavor suddenly becomes more populated than the others. When the majority flavor reaches $\nu_\alpha = 1$, the other flavors are reset to the vicinity

of the charge neutrality point, and then begin filling again equally as the density is raised, until another phase transition is encountered. This is the cascade of revivals described in Refs [1,2].

In Fig. S3b, we present the entropy per unit cell $s(\nu, T)$ computed from the same model, as a function of ν for different temperatures. Thus, the entropy show clearly the revival transitions, visible as sharp dips in the entropy near each integer filling. The dips are explained by the fact that the total density of states at the Fermi level is minimal at these fillings. This ν dependence of the entropy resembles the one measured at a high field, $B_{\parallel} = 12\mathrm{T}$ (Fig. 2e), suggesting that the mean-field description captures the essential part of the physics there. On the other hand, the entropy measured at $B_{\parallel} = 0\mathrm{T}$ (fig. 2e) is quantitatively different than the one obtained here, emphasizing the imporant role of fluctuating free moments which are not included in the mean-field model.

We note that the partial fillings as a function of ν at the elevated temperatures are not strongly modified compared to those at $T = 0$, shown in Fig. S3a, although the positions of the phase transitions shift slightly with temperature.

SI4. The effect of a magnetic field on the entropy in a mean-field model without free spins

A Zeeman field can be included in the Hamiltonian (4) by adding the following term:

$$H_Z = -E_Z \sum_{\mathbf{k},\alpha,n} \sigma_\alpha \, \psi^\dagger_{\alpha n \mathbf{k}} \psi_{\alpha n \mathbf{k}}, \tag{8}$$

where $E_Z = \mu_B B_{\parallel}$ is the Zeeman energy, and σ_α is the spin projection of electrons of flavor α along the magnetic field. To account for the Zeeman field in the mean-field calculation, we replace $\mu \to \mu + E_Z \sigma_\alpha$ in Eqs. (6) and (7).

The entropy vs. ν at $T = 10\mathrm{K}$ in the presence of different in-plane magnetic fields is shown in Fig. S4. As seen in the figure, the effect of a field of up to $B_{\parallel} = 12\mathrm{T}$ is quite small, decreasing the entropy by at most $0.1 k_B$ relative to the $B_{\parallel} = 0$ value near the maxima of the

entropy before the integer fillings. The change in the entropy away from the maxima due to the field is even smaller.

Comparing the mean-field results to the experimentally measured entropy (Fig. 2e in the main text), we see that the calculated entropy is in rough qualitative agreement with the experimental one at $B_{\parallel} = 12\mathrm{T}$ and $T \approx 10\mathrm{K}$, showing a similar peak structure near each integer filling. The overall magnitude of the calculated entropy at $B_{\parallel} = 12\mathrm{T}$ is also similar to the measured one. However, the calculated entropy at $B_{\parallel} = 0$ is very different from the measured entropy. In particular, unlike in the calculation, the measured entropy does not drop after $\nu = 1$, but rather remains nearly constant at a high value. Moreover, the measured entropy is strongly field dependent for $\nu > 1$, whereas the calculated one is weakly field dependent at all ν. We ascribe this failure of the mean-field model to the appearance of nearly-free magnetic moments (as discussed in detail in the main text). These free moments, that onset near $\nu = 1$, fluctuate strongly at low magnetic fields, an effect which is not captured in mean-field theory. Upon applying a strong Zeeman field, these fluctuations are quenched (as seen experimentally by the dramatic decrease in the entropy), and mean-field theory may be adequate.

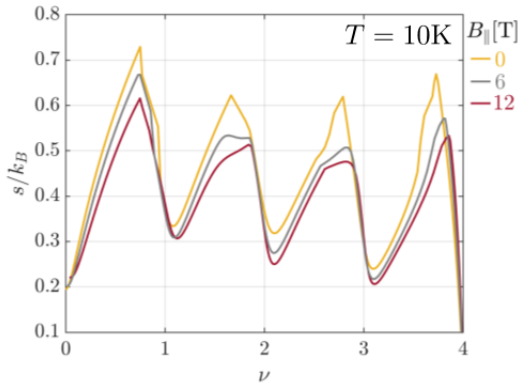

Figure S4: Effect of an in-plane magnetic field on the entropy within the mean-field model. In this calculation, the temperature is $T = 10\mathrm{K}$. The different curves are for $B_{\parallel} = 0\mathrm{T}, 6\mathrm{T}, 12\mathrm{T}$. The entropy depends only weakly on field, in contrast to the experiment. As explained above, the mean-field approximation does not capture the strong magnetic fluctuations present in the experiment at $\nu > 1$.

SI5. Tracking ν_R using different features of the $d\mu/dn$ jump

In the main text, the transition from high to low compressibility near $\nu = 1$ was tracked by following the midpoint of the rise in $d\mu/dn$. Since the rise is fastest around its midpoint, this procedure gives us excellent resolution in defining the filling factor that corresponds to this rise, of about $\delta\nu_R \sim 0.005$. We note, however, that the overall width of the rise in filling factor can be significantly larger, and in extreme cases can even reach $\Delta\nu \approx 0.2$. It is thus necessary to check whether tracking different features of the transition as a function of magnetic field or temperature will lead to similar conclusions.

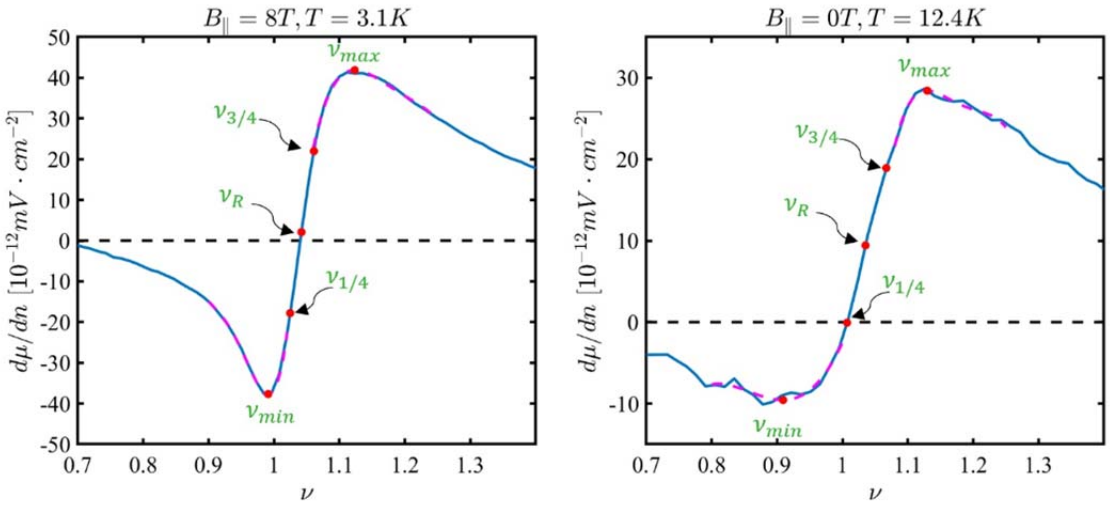

Fig. S5: $d\mu/dn$ rise at for different T, $B_\parallel$. a. Measured rise in $d\mu/dn$ near $\nu = 1$ at $B_\parallel = 8\text{T}$ and $T = 3.1\text{K}$**. b.** Same for $B_\parallel = 0\text{T}$ and $T = 12.4\text{K}$. The filling factors that correspond to the minimum and maximum of the rise, ν_{min} and ν_{max} are identified using a fit to a 4th order polynomial around the relevant regions (dashed purple). Also labeled are the filling factors at the midpoint of the rise, ν_R, at quarter of the rise, $\nu_{1/4}$, and at three quarters of the rise, $\nu_{3/4}$.

In Fig. S5 we show two examples: the first (panel a), measured at $B_\parallel = 8\text{T}$ and $T = 3.1\text{K}$, shows a rather sharp rise. In the second (panel b), measured at $B_\parallel = 0\text{T}$ and $T = 12.4\text{K}$, the rise is more gradual. In general, similar to what is shown in these two representative measurements, we see that lower fields or higher temperatures smear the $d\mu/dn$ rise. To check how sensitive are the results shown in Fig. 4 of the main text to the choice of the

definition of the location on the rise in $d\mu/dn$, we repeat the analysis with different criteria for the chosen location. Since ν_{min} and ν_{max} have large uncertainties, especially at high temperatures and low fields, we follow instead the filling factors at one quarter of the rise, $\nu_{1/4}$, and three quarters of the rise, $\nu_{3/4}$. The uncertainties in determining the latter are still low enough to make significant observations, and their tracking can still identify whether the observed features are tied to a specific part of the rise. Fig. S6 shows the extracted $\nu_R, \nu_{1/4}$, $\nu_{3/4}$ and $\nu_{d\mu/dn=0}$, plotted as a function of T at $B_{\parallel} = 0\mathrm{T}$ and $B_{\parallel} = 12\mathrm{T}$. This figure should be compared with Fig. 4d in the main text.

While there are quantitative difference between the curves obtained by the different methods, we can see that in the overall dependence and the essential features in all the curves agree. For example, we see that at $B_{\parallel} = 12\mathrm{T}$, independently of the method used, ν_R increases with temperature at low temperatures, reaching a maximum, and then starts decreasing with increasing temperature at high temperatures, where the crossover occurs at $T \approx 9\mathrm{K}$.

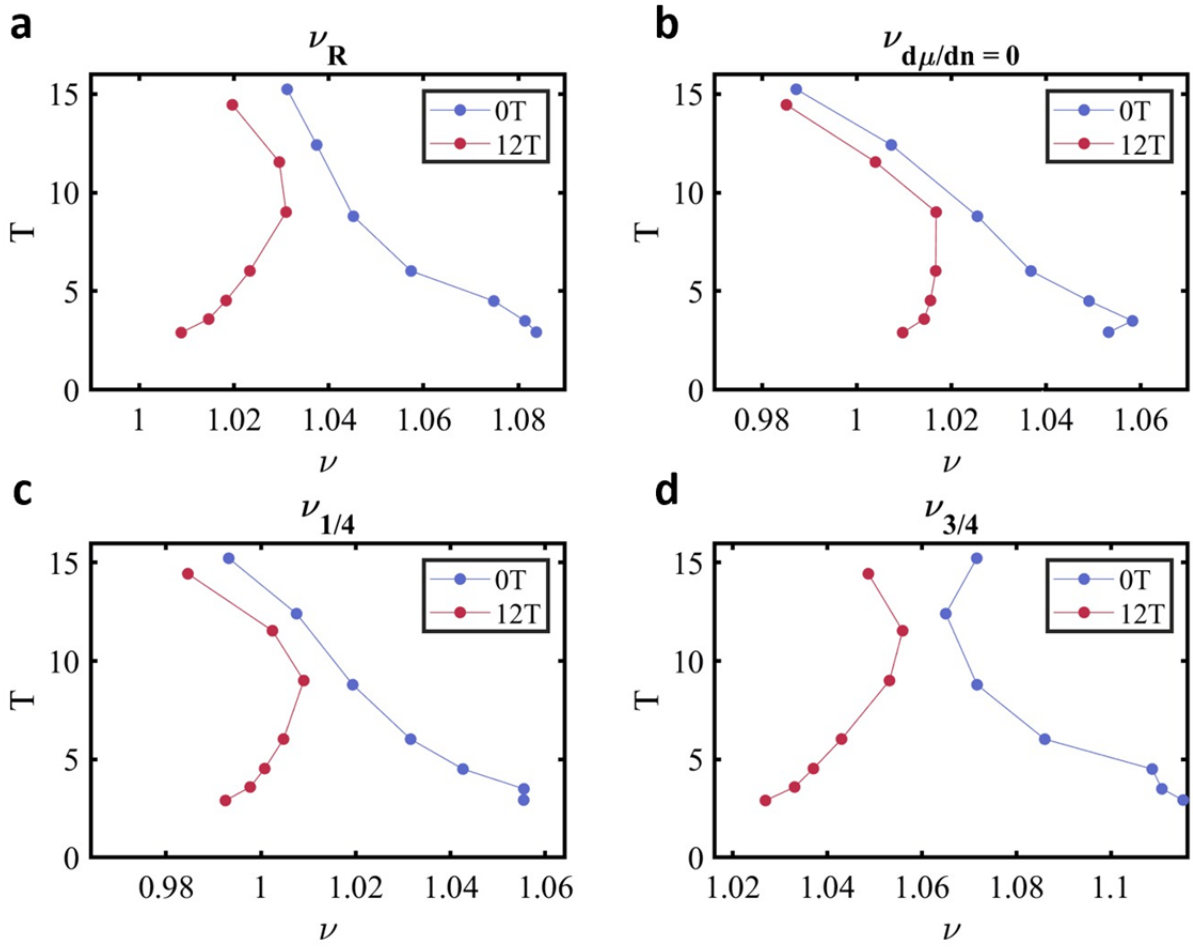

Fig. S6: Tracking different features of the $d\mu/dn$ rise near $\nu = 1$. a. ν_R, **b.** $\nu_{d\mu/dn=0}$, **c.** $\nu_{1/4}$, **d.** $\nu_{3/4}$ (as defined in Fig. S5 and in this section's text) as a function of $B_\parallel$ and T.

SI6. Thermodynamic model for Fermi liquid to free moment phase transition

Here, we describe the simple thermodynamic model we used in the main text to describe the first order phase transition.

The experiment is done under conditions where the temperature T, parallel magnetic field $B_\parallel$, and gate voltage v_g are fixed. The appropriate thermodynamic potential to be minimized under these conditions is the grand canonical potential, $\Omega(v_g, T, B_\parallel)$. It is convenient to express the gate voltage in terms of the equivalent filling factor, $\nu_0 = \frac{1}{e} c_g v_g$ (c_g is the geometric capacitance from the MATBG to the gate per moiré unit cell). For clarity, it is useful

to derive the grand canonical potential starting from the free energy f, which is a function of the filling factor ν, and then obtain Ω by a Legendre transformation.

Our simple model postulates the existence of a first order transition between two phases. The first phase is a relatively simple metallic phase, which we model as a Fermi liquid. The second phase is characterized by the existence of free moments. This phase is also metallic, although its density of states is lower than that of the first phase. We assume that in the second phase, there is one free spin per unit cell, coexisting with metallic Fermi liquid electrons.

The free energies per moiré unit cell of the two phases are chosen as follows:

$$f_i(\nu, T, B_\parallel) = \varepsilon_i + \frac{1}{2}\left(\frac{e^2}{c_g} + \frac{1}{\kappa_i}\right)\nu^2 - \mu_i\nu - \frac{\gamma_i T^2}{2} - \frac{\chi_i B_\parallel^2}{2} - \alpha_i T \ln\left[2\cosh\left(\frac{\mu_B B_\parallel}{T}\right)\right].$$

Here, $i = 1{,}2$ labels the two phases, ε_i and μ_i are reference energies and chemical potentials, $\kappa_i = \left(\frac{dn}{d\mu}\right)_i$ are the intrinsic compressibilities (or quantum capacitances), $\gamma_{1,2}$ are the specific heat coefficients, χ_i are the Pauli contributions to magnetic susceptibility of the itinerant electrons, and α_i are the concentrations of free spins per unit cell, taken to be $\alpha_1 = 0$ and $\alpha_2 = 1$ (the results do not depend sensitively on the value of α_2, as long as it is of order unity). We have assumed that the free spins have a gyromagnetic ratio $g = 2$.

We now carry out a Legendre transformation, $\Omega = f - ev_g\nu$, minimize Ω with respect to ν, and thus eliminate ν in favor of $\nu_0 = \frac{1}{e}c_g v_g$. Since in our experiment e^2/c_g is much larger than $1/\kappa_i$, we keep only terms to lowest order in $\frac{c_g}{e^2\kappa_i}$. The grand potentials of the two phases per unit cell are:

$$\Omega_i(\nu_0, T, B_\parallel) = \tilde{\varepsilon}_i - \frac{1}{2}\frac{e^2}{c_g}\nu_0^2 - \mu_i\nu_0 - \frac{\gamma_i T^2}{2} - \frac{\chi_i B_\parallel^2}{2} - \alpha_i T \ln\left[2\cosh\left(\frac{\mu_B B_\parallel}{T}\right)\right].$$

Here, $\tilde{\varepsilon}_i = \varepsilon_i - \frac{c_g}{2e^2}\mu_i^2$. In terms of $\Omega(\nu_0, T, B_\parallel)$, the thermodynamic variables are given by:

$$\nu = -\frac{c_g}{e^2}\frac{\partial\Omega}{\partial\nu_0},\ s = -\frac{\partial\Omega}{\partial T},\ m = -\frac{\partial\Omega}{\partial B_\parallel},$$

where s and m are the entropy and in-plane magnetization per unit cell, respectively.

The first order transition surface in the $(\nu_0, T, B_\parallel)$ parameter space is given by the condition $\Delta\Omega(\nu_0, T, B_\parallel) = \Omega_2 - \Omega_1 = 0$. The theoretical curves shown in Fig. 4 of the main text were obtained using the following parameters: $\tilde{\varepsilon}_2 - \tilde{\varepsilon}_1 = 72\mathrm{K}$, $\mu_2 - \mu_1 = 64\mathrm{K}$, and $\gamma_2 - \gamma_1 = -0.0331K^{-1}$. The negative sign of $\gamma_2 - \gamma_1$ corresponds to the fact that the density of states of itinerant carriers in the free moment phase is lower than that of the simple metallic phase. For simplicity, we neglect the Pauli contribution χ_i to the magnetic susceptibility, which is negligible compared to the free moment contribution.

Under these assumptions, the surface of the first order transition can be simply expressed as:

$$\nu_0^* = \frac{1}{\mu_2 - \mu_1}\left\{\tilde{\varepsilon}_2 - \tilde{\varepsilon}_1 - \frac{1}{2}(\gamma_2 - \gamma_1)T^{*2} - T^* \ln\left[2\cosh\left(\frac{\mu_B B_\parallel^*}{T^*}\right)\right]\right\},$$

where ν_0^*, T^*, and $B_\parallel^*$ denote the equivalent filling factor, temperature, and magnetic field of a point on the transition surface.

The Clausius-Clapeyron relations along the transition surface can be obtained by differentiating $\Delta\Omega$:

$$d\Delta\Omega = -\frac{e^2}{2c_g}\Delta\nu d\nu_0^* - \Delta s dT^* - \Delta m dB_\parallel^*.$$

Here, $\Delta\nu = \nu_2 - \nu_1$, $\Delta s = s_2 - s_1$, and $\Delta m = m_2 - m_1$ are the jumps in the filling factor, entropy, and magnetization across the transition, respectively. Along a $\nu_0^* = const.$ contour of the transition surface, get the relation

$$\left(\frac{\partial T^*}{\partial B_\parallel^*}\right)_{\nu_0^*} = -\frac{\Delta m}{\Delta s},$$

which is the relation we used in SI7, with ν_0^*, T^*, and $B_\parallel^*$ identified as the filling factor (ν_R), temperature, and magnetic field at the Dirac revival point.

SI7. Anti-correlation between entropy and magnetization.

The jump in compressibility seen at ν_R is sharp, but not discontinuous, as one may naively expect from a first order phase transition. Indeed, in the presence of long-range Coulomb interactions and disorder in two dimensions, a first order transition is not expected to be sharp. If we assume that the revival transition at $\nu = 1$ represent a smeared first-order phase transition, we can derive from the shape of the phase boundary the relation between magnetization and entropy. We demonstrated this relation by analyzing the slope of the phase boundary via the Clausius-Clapeyron equation: $\Delta m/\Delta s = -(\partial T/\partial B_{\parallel})_{\nu_R}$. Here, Δs and Δm are the differences in the entropy and magnetization per moiré unit cell between the free moment and the Fermi liquid phases, and $(\partial T/\partial B_{\parallel})_{\nu_R}$ is the derivative of the transition temperature with respect to magnetic field at constant ν_R. To obtain the ratio $\Delta m/\Delta s$ we reconstruct such equi-ν_R contours by fitting a polynomial surface in the $B_{\parallel}$ and T plane to the measured points, and extract the slope of the contour lines at different points (Fig. S7). Consider point A in Fig. S7: At this point, $(\partial T/\partial B_{\parallel})_{\nu_R} \approx 0$. The Clausius-Clapeyron equations then imply that $\Delta m \approx 0$. In contrast, at point B, the equal ν_R contours are nearly vertical, implying that $\Delta s \approx 0$. This clear anti-correlation between Δs and Δm follows naturally from our simple model, where both Δs and Δm originate from the same free moments, that are either strongly thermally fluctuating, or polarized along the magnetic field. At point C, the contour has a positive slope, from which we deduce that $\Delta s < 0$, $\Delta m > 0$.

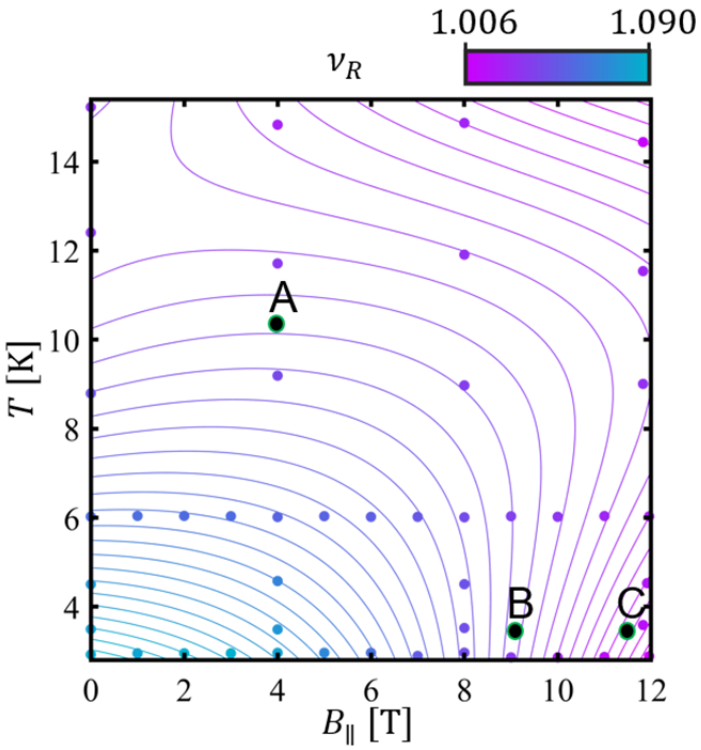

Fig. S7: Anti-correlation between the entropy and magnetization as determined from the boundary surface curvature. Measured ν_R as a function of $B_\parallel$ and T (colored dots). The contours are obtained from a fit of these dots to a polynomial surface (3rd order in T and 2nd order in $B_\parallel$). The slope of the contours in this $(B_\parallel, T)$ plane gives via the Clausius-Clapeyron relation the ratio of the magnetization and entropy jumps across the transition, $\Delta m/\Delta s = -(\partial T/\partial B_\parallel)_{\nu_R}$. Visibly, in the point labeled A the contours are horizontal, implying $\Delta m \approx 0$. At point B the contours are vertical and thus $\Delta s \approx 0$. The crossover occurs along a diagonal line that correspond to the polarization of the free moments. At point C, the contour has a positive slope, from which we deduce that $\Delta s < 0$, $\Delta m > 0$.

SI8. Comparison of transport measurements and compressibility.

Using the multilayer device shown in Fig. 3a, we can simultaneously obtain the transport resistances and the chemical potential of MATBG. Fig. S8a shows the longitudinal resistance R_{xx} versus ν at different temperatures from $1\mathrm{K}$ to $70\mathrm{K}$. The peaks in resistance near $\nu = -1$ denoted by the blue dots start appearing at a finite temperature of $\sim 5\mathrm{K}$, and subsequently move to lower absolute value of filling factor as the temperature increases. The Hall coefficient and density, as shown in Fig. S8b and c, also show a similar trend. The shift of the resistive peak at $\nu = -1$ has been attributed[3] to a Pomeranchuk-like mechanism, similar to the one near $\nu = 1$.

The shift of the peak at $\nu = +1$, on the other hand, is much smaller, as was also observed in Device 1 shown in Fig. 1. Indeed, from our analysis in Fig. 4, the shift of the $\nu = +1$ state as a function of temperature is on the order of $\Delta\nu = 0.06$, which might be shadowed in the transport measurement by a moderate twist angle inhomogeneity on the order of ±0.02°.

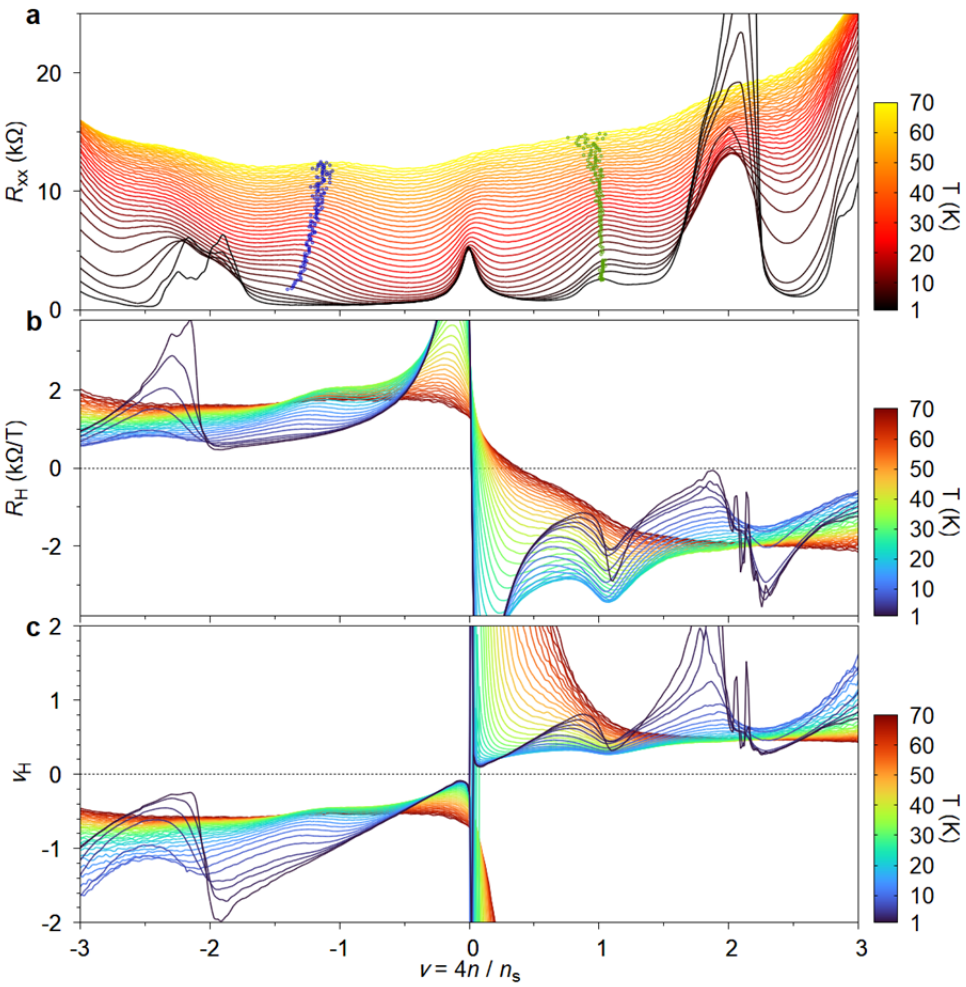

Figure S8: Transport characterization of MATBG from $1 - 70\mathbf{K}$. (a) Longitudenal resistance R_{xx} versus ν. Blue and green dots mark the peaks in resistance near $\nu = \pm 1$ after a linear background is removed at each temperature. (b-c) Hall coefficient $R_H = dR_{xy}/dB$ and the corresponding Hall density $\nu_H = (-\frac{1}{R_H e})/(\frac{n_s}{4})$ in the same range of temperatures and densities.

SI9. Comparison of the temperature dependence of $d\mu/dn$ near $\nu = 1$ and $\nu = -1$.

As discussed in the main paper there are qualitative similarities between the measurements of the entropy in the electron and hole sides, although the system is far from being electron-hole symmetric. In figure S8a we present a measurement of $d\mu/dn$ as a function of filling factor for different temperatures, covering both the electron and hole sides. As can be seen in the figure, an asymmetric "Dirac revival" jump in the compressibility is present in both the electron and hole sides. However, while the jump of $d\mu/dn$ in the electron side is very sharp and appears close to $\nu = 1$, in the hole side it is much broader, smaller in height, and appears further away from $\nu = -1$. The fact that the Dirac revival features in the compressibility is stronger and sharper on the electron side have already been observed in earlier experiments[1] over a wide range of twist angles.

Although the feature in the hole side is more smeared than that in the electron side, the temperature dependencies of the two features are qualitatively similar: both become stronger and move towards charge neutrality with increasing temperature (see also Fig. S8b). This suggests that the underlying physics in the vicinity of $\nu = \pm 1$ may be similar. However, the reason for the large width of the feature on the hole side is currently unclear. Potential disorder is expected to smear the electron and hole sides in a similar way, and therefore it cannot explain the difference between the widths in the two sides. Angle disorder can also lead to a spatial smearing of the local filling factor, $\nu = n/(n_s/4)$, by locally varying the density that corresponds to full flat bands, n_s. However, also this effect should be electron-hole symmetric for $\nu = \pm 1$, since the absolute value of the carrier density in these two filling factors is the same. One can also clearly see that the combined effect of potential and angle disorder is rather small, since even in their presence the jump of $d\mu/dn$ in $\nu = +1$ is very sharp. A possible reason for the difference might be that the density jump between the two phases that are involved in the transition is larger in the hole side than in the electron side, and therefore the density range of mesoscale phase coexistence in the hole side is larger. However, this is purely speculative, and more experiments would be needed to clarify the underlying reasons for the differences between the physics in the conduction and valence flat bands.

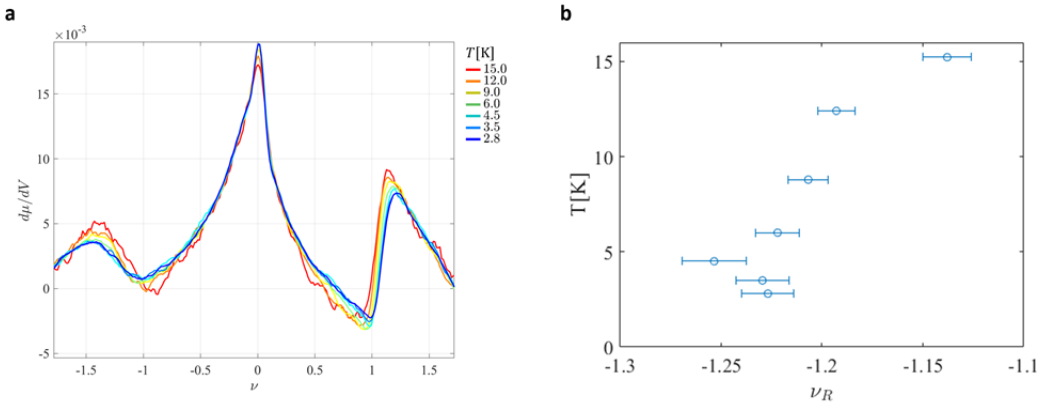

Figure S8: Comparison of the temperature dependence of $d\mu/dn$ near $\nu = 1$ and $\nu = -1$. a. $d\mu/dn$ measured as a function of ν at various temperatures. **b.** The filling factor that corresponds to revival transition near $\nu = -1$, ν_R, determined by the deflection point of the rise in $d\mu/dn$, plotted as a function of temperature.

SI10. The nature of the revival transition near $\nu = 1$

The central finding of this work is the identification of two regions in the phase diagram with very distinct behaviors of the entropy. The jump in compressibility as a function of density that separates the two regions is quite sharp; however, the jump is not infinitely sharp and is not resolution limited. In addition, there is no sign of hysteresis between the two regions. Therefore, strictly speaking, there is no first-order transition between the two regions. This is not unexpected, since as we point out in the manuscript, first-order transitions are not allowed in two dimensions in the presence of disorder and long-range Coulomb interactions. This is so since in the vicinity of the transition the system always prefers to break up into mesoscopic domains of the two phases, smearing the transition. The length scale over which the system breaks up depends strongly on microscopic parameters. In similar systems where disorder induces phase separation the typical spatial scale of the domains is of the order of tens of nanometers (for a recent example see Ref [4]), well below our spatial resolution (which was about 500nm in this experiment). Thus, although the transition is rather sharp we cannot rule out the possibility that this is a sharp crossover rather than a 1st order phase transition. In our experiment, there is no evidence for a spontaneously broken symmetry in the $\nu > 1$ phase at temperatures $T > 2.8\,\mathrm{K}$. Conversely, at these temperatures the magnetic moments in this phase are strongly fluctuating, showing no sign of long-range order. Thus, a smooth crossover between the two phases is not forbidden and can be consistent with the data. Nevertheless, since the crossover is quite rapid, it seems reasonable to interpret it as a slightly smeared underlying first order transition, and we show that such an interpretation naturally explains the dependence of the phase boundary on temperature and in-plane field.

A higher-order transition is also possible, but on theoretical grounds, we believe it is less likely. A second-order transition can occur generically between two phases that are distinguished by symmetry; however, as mentioned above, there is no direct evidence in our experiment for spontaneous symmetry breaking at $T > 2.8\mathrm{K}$. Alternatively, a second-order transition may appear as a critical end point of a first order transition (as in a liquid-gas critical point). However, this critical point requires fine tuning, and should appear as a point in the (ν, T) plane, rather than as a line.

We also note that hysteretic behavior is not forbidden near specific phase transitions in two-dimensions. For example, hysteresis was observed near $\nu = -1$ in references [10] and [13] of the main paper. In those works, the system was measured in the presence of a perpendicular magnetic field, while our experiments are performed in an in-plane field. In addition, the hysteresis was observed there upon cycling the magnetic field (and not the density), whereas our scans were only taken as a function of density. Finally, the hysteresis was visible only at low temperatures ($T < 1\mathrm{K}$), whereas our experiments are done at $T > 2.8\mathrm{K}$.

Often, the existence of hysteresis is tied to the presence of an incompressible phase in the system. In the vicinity of an incompressible phase and in the presence of disorder, it is well known that the system breaks up in real space to incompressible and compressible regions. Compressible islands that are surrounded by incompressible strips can have very long charging times, and this leads to glassy behavior of the overall system. This can manifest itself in hysteresis, as is seen, e.g., around quantum Hall gapped states (for a recent example, see Fig. S5 in https://arxiv.org/pdf/2008.05466.pdf). On the other hand, if the phases that are involved are compressible, charge can equilibrate rapidly. Thus, hysteresis that is related to the ability of the charge degrees of freedom to equilibrate will happen only when a gapped phase is involved. This could explain very nicely the difference between our experiment and those of Refs. [10,13]: in these references, hysteresis is observed whenever a Chern insulator appears. Since a Chern insulator is gapped, the formation of a real space mixture of a Chern insulator and a compressible phase can cause hysteresis. In our experiment, in contrast, there is no indication for a thermodynamic gap, and the two phases on either side of the transition are clearly compressible, which can explain the absence of hysteresis in our case.

Hysteresis can, in principle, also arise due to the formation of a macroscopic collective degrees of freedom, such as domain walls in a ferromagnet, whose equilibration time can be very long. This situation arises naturally, for example, when there is a spontaneous breaking of a discrete symmetry. However, in our experiment, performed at $T > 2.8\mathrm{K}$, there is no indication for such symmetry breaking.

SI11. The entropy data at two temperature windows

The $\sim 10K$ temperature range used for extracting the entropy in this paper was necessary for obtaining low enough noise, such that the entropy curves have good significance. With our existing signal-to-noise ratios it would be prohibitive to measure the detailed temperature dependence of the entropy. Nevertheless, to check the consistency of our data we bin it below into two temperature windows. Figure 9 shows the 'magnetic entropy', $S(0T) - S(12T)$, similar to the one shown in the paper (Fig. 2e, inset), but now extracted from two separate temperature windows: $T = 3.5K - 9K$ and $T = 9K - 16K$. The shaded regions around each curve show the error bars, determined in a similar manner to those in the main paper (as described in the Supplementary Information section SI1). Notably, there are some differences between the two curves. However, these differences are well within the error bars, and thus we do not think one can assign a real significance to them. On the other hand, we can see that the two entropy traces, obtained from the two different temperature windows, look overall very similar. Specifically, both curves show a rather sharp increase of the 'magnetic entropy' near $\nu = 1$ and a fast decrease near $\nu = 2$. This gives additional support to the robustness of our observations, but also lends extra support to the observation that we made in the paper, based on the mapping of the phase boundary (Fig. 4), that the 'magnetic entropy' appears already at very low temperatures, of the order of few degrees Kelvin.

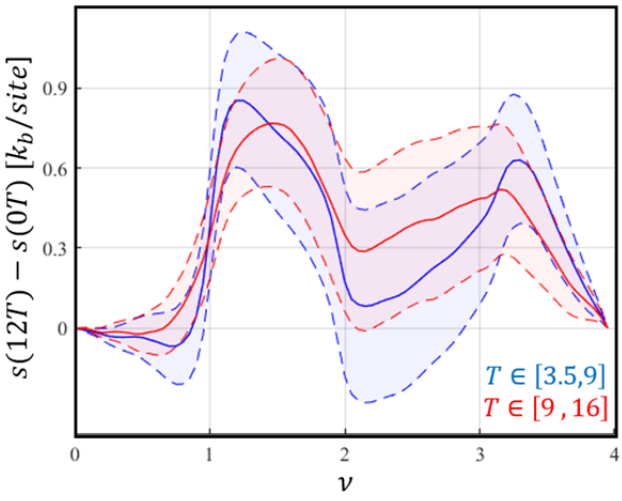

Figure S9: Magnetic entropy from two temperature windows. a. The magnetic entropy, $s(12T) - s(0T)$, extracted from the slope of μ vs. T taken at from two different temperature windows: $T = 3.5 - 9K$ (blue) and

462 $T = 9 - 16K$ (red). The shaded regions indicate the error bars, determined along the same procedure used for Fig.
463 2e in the main paper, that is described in section SI1.

464

465 1. Zondiner, U. *et al.* Cascade of phase transitions and Dirac revivals in magic-angle
466 graphene. *Nature* **582**, 203–208 (2020).

467 2. Park, J. M., Cao, Y., Watanabe, K., Taniguchi, T. & Jarillo-Herrero, P. Flavour Hund's
468 Coupling, Correlated Chern Gaps, and Diffusivity in Moir'e Flat Bands. *Arxiv* 2008.12296
469 (2020).

470 3. Saito, Y. *et al.* Isospin Pomeranchuk effect and the entropy of collective excitations in
471 twisted bilayer graphene. *ArXiv* 2008.10830 (2020).

472 4. Tilak, N. *et al.* Flat band carrier confinement in magic-angle twisted bilayer graphene.
473 *preprint at ResearchSquare* (2020). doi:10.21203/rs.3.rs-88276/v1

474